

Topological quantum cascade laser with Dirac-scaled valley edge modes

Received: 4 February 2025

Accepted: 10 November 2025

Published online: 11 December 2025

 Check for updates

Yunda Chua^{1,7}, Letian Yu^{2,7}, Jieyuan Cui^{1,7}, Bofeng Zhu², Hanyu Liu¹, Qian Wang³, Zhipeng Li⁴, Lianhe Li⁵, Alexander Giles Davies⁵, Edmund Harold Linfield⁵, Baile Zhang^{2,6} ✉ & Qi Jie Wang^{1,2} ✉

Topological lasers, born from the fusion of topological physics and lasing theory, offer an unprecedented mechanism to achieve coherent lasing. By utilizing topologically protected boundary states, they exhibit robustness against defects and imperfections. However, this mechanism faces a fundamental limitation: while relying on the bulk of a photonic topological insulator for topological protection, the lasing modes, defined as boundary states, must be evanescently confined to the boundary, leading to severely limited mode volume. Here, using the platform of topological quantum cascade lasers previously demonstrated with valley edge states, we demonstrate a substantial expansion of the lasing mode volume under topological protection. Unlike conventional designs, we introduce an additional bulk region featuring gapless Dirac points at the interface between topologically distinct domains. This Dirac region enables the topological lasing mode to uniformly extend across the entire region, dramatically increasing the lasing mode volume. The scaled-up mode volume enhances the robustness of the laser against defects of comparable size, outperforming unscaled designs. Our results resolve a fundamental challenge in topological laser design and also contribute to the development of cutting-edge quantum cascade lasers with enhanced efficiency and robustness.

Topological lasers represent an emerging frontier in photonics by integrating the concepts of topological insulators and coherent photon emission^{1–5}. In condensed matter physics, topological insulators are phases of matter in which the bulk is insulating but the edges or surfaces exhibit robust conductance due to the topological boundary states^{6–8}. In photonics, topological lasers utilize the photonic counterparts of topological insulators, known as photonic topological insulator, to realize highly stable light generation^{9,10}; by incorporating optical gain into those photonic topological boundary modes, one can

realize robust lasing that is intrinsically protected against back-scattering from defects and disorder^{11–20}. This unique interplay between topological physics and photon emission lies at the heart of topological lasers, opening pathways toward compact, defect-tolerant light sources with potential applications in spectroscopy, communication, and integrated photonics^{1,2}.

Despite their technological promise, the transition of topological lasers from conceptual demonstrations to practical applications remains hindered by fundamental challenges. At the core of

¹Centre for OptoElectronics and Biophotonics, School of Electrical and Electronic Engineering & The Photonics Institute, Nanyang Technological University, Singapore, Singapore. ²Division of Physics and Applied Physics, School of Physical and Mathematical Sciences, Nanyang Technological University, Singapore, Singapore. ³Institute of Materials Research and Engineering, Agency for Science, Technology and Research (A*STAR), 2 Fusionopolis Way, #08-03, Innovis, Singapore, Singapore. ⁴School of Material Science and Engineering, Central South University, Changsha, China. ⁵School of Electronic and Electrical Engineering, University of Leeds, Leeds, UK. ⁶Centre for Disruptive Photonic Technologies, Nanyang Technological University, Singapore, Singapore. ⁷These authors contributed equally: Yunda Chua, Letian Yu, Jieyuan Cui. ✉ e-mail: blzhang@ntu.edu.sg; qjwang@ntu.edu.sg

topological physics is the bulk–boundary correspondence principle²¹, which dictates that the nontrivial band topology of the bulk gives rise to topologically protected boundary states. While this principle provides robustness against scattering and fabrication imperfections, it also requires the lasing mode, as a boundary state, to be evanescently confined to the boundary. As a result, a large portion of the bulk remain ‘inactive’ for laser emission, and the limited volume of topological edge modes constrains the amount of light power that can be harvested.

Quantum cascade lasers (QCLs)^{22–25} are promising platforms for exploiting the topological edge mode lasing due to their semiconductor nature and compactness²⁶. Among the various topological concepts explored for topological QCLs^{27–29}, one of the most notable for demonstrating topological properties such as robustness to defects is the valley photonic crystal design. A valley in a bandstructure refers to a local minimum/maximum of an upper/lower band separated by a bandgap, usually occurring at a high-symmetry point of the Brillouin zone³⁰. The valley degree of freedom (DOF) first gained prominence in condensed matter physics in the context of valleytronics³¹. Valley photonic crystals were later introduced into lasers, giving rise to the first electrically pumped topological laser¹⁹. However, the pumping efficiency power was limited as only edge-modes regions were pumped. As a result, despite the intrinsic advantages offered by topological photonics for robust operation, a substantial gap remains between current topological QCL implementations and the practical requirements for THz radiation sources²⁵.

Here, we demonstrate a topological QCL with a substantially expanded lasing mode volume. This expansion is achieved by introducing an additional bulk region exhibiting Dirac point degeneracies at the interface between two photonic domains with opposite valley-Hall (VH) topologies. Building upon the celebrated valley Hall edge states^{32–38}, here we demonstrate their transition into ‘valley Hall bulk states’ while preserving the topological properties. The topological lasing mode is no longer a conventional topological boundary mode, but a hybridized mode that uniformly extends across the entire Dirac bulk region, which we term the Dirac-scaled topological mode. Our experimental results show regularly spaced emission peaks, consistent across multiple samples, and indicative of running wave modes in the Dirac-scaled cavity. Further cover-plate measurements reveal a uniform mode distribution throughout the Dirac bulk region, highlighting the increased mode volume enabled by our design. Finally, we assess the robustness of the Dirac-scaled design, in light of recent concerns regarding the vulnerability of VH topological waveguides to common structural imperfections^{39–41}. By deliberately introducing multiple defects of comparable size into both the scaled and unscaled devices, we observe a clear contrast in the lasing performance: while the unscaled structure undergoes serious mode localization due to the defects, the scaled configuration maintains mode circulation, demonstrating a significant enhancement in robustness. This finding underscores the potential of Dirac-scaling to mitigate the fragility often observed in valley topological systems, further strengthening the applicability of topological photonics in real-world terahertz applications.

Results

Device structure

The QCL active region is fabricated into a double-metal waveguide, which supports only the transverse magnetic (TM) polarized mode due to the dipole selection rule. The photonic crystal pattern etched into the QCL consists of three distinct regions, as shown in Fig. 1a, b. The core of the scaled VH waveguide is formed using lattice unit with C_6 rotational symmetric hexagonal shaped air-hole. Owing to its inversion symmetry, the scaled region hosts a pair of Dirac points at K and K' valleys at -3.35 THz. This region is then electrically pumped to provide

gain to the guided VH modes. On either side of the waveguide, electrically isolated lattices with C_3 rotational symmetry hexagonal air holes exhibit opposing valley Chern numbers of ± 0.5 . As a result, the waveguide supports a guided VH dispersion band, as shown in Fig. 1c, due to its nonzero valley Chern number^{42–44}. The unit cell used in our device has a lattice constant of $a = 16.77 \mu\text{m}$. The degree of asymmetry in the hexagonally shaped gapped lattice is optimized to maximize the bandgap opening, with the shorter and longer sides denoted as $d_1 = 2.33 \mu\text{m}$ and $d_2 = 11.58 \mu\text{m}$. This parameter choice enables a band gap spanning from 3.02 to 3.45 THz.

In contrast, for the gapless Dirac lattice, the hexagonal air hole has equal-length sides with $d_{1,2} = 7.08 \mu\text{m}$. The unit cell parameters and structure can be found in Fig. 1a, and their respective dispersion details are presented in Supplementary Fig. 1a in the Supplementary Materials. We stress that our approach differs from earlier studies focused on homogeneous photonic crystals with Dirac dispersions^{45–47} or transport experiments in acoustic and microwave waveguide systems^{48–51}. Instead, our central objective is to explore whether lasing performance can be scaled while preserving the robust characteristics afforded by topological protection.

Our VH waveguide is structured into a triangular-loop-shaped optical cavity^{19,52}, where the sharp corners serve as a stringent test to confirm the topological characteristics of cavity modes. Unlike trivial modes, topological modes are immune to scattering at these corners⁵³. The degree of scaling is quantified by the number of Dirac lattices spanning the waveguide width, denoted as D_{Dirac} (Fig. 1b). The total number of defects within the cavity is represented by N_{Defect} . These defects are introduced to assess the uniformity and circulation properties of the guided mode by scattering a fraction of the in-plane radiation toward the out-of-plane Fourier transform infrared spectroscopy (FTIR) detection window. All fabricated devices maintain a consistent size for the inner region enclosed by the waveguide. As the waveguide is scaled, the increasing width of the topological waveguide extends outward toward the device boundary. The pump regions are carefully designed to cover most of the mode area while remaining confined to the perimeter of the Dirac lattices, thereby minimizing excessive heat generation and the excitation of bulk modes outside the waveguides (electrical simulation shown in Supplementary Fig. 13 in the Supplementary Materials). In unscaled devices with $D_{\text{Dirac}} = 0$, where Dirac lattices are not used in the waveguide, simulation results show that a width of five lattice units is sufficient to excite the valley edge mode¹⁹. In the $D_{\text{Dirac}} = 3$ and $D_{\text{Dirac}} = 6$ cavities, the pump region is slightly increased, with pump widths of six and seven lattice units, respectively, to accommodate the broadened mode area in each case.

By analyzing the measured spectral and intensity characteristics, we can evaluate the robustness of cavity modes to perturbations across different scaling designs. To facilitate localized spectral measurements at individual defect sites, metal cover plates were employed to suppress surface emissions from other regions of the cavity during experiments (schematic illustrations shown in Supplementary Fig. 5 in the Supplementary Materials). The defects were strategically spaced to minimize spectral overlap, ensuring clean and independent measurements.

Mode uniformity

A distinctive feature of Dirac-scaled VH modes, compared to other non-topological guided modes, is their relatively uniform mode envelope across the waveguide width within the region of Dirac lattices (see Fig. 1d). As such, probing the mode's field distribution within the cavity is crucial for verification. Due to the electrical, cryogenic, and vacuum conditions required for the operation of THz QCLs, conventional near-field measurements are inaccessible. Thus, we introduce rectangular, wavelength-sized defects, randomly placed along and across the waveguide in the scaled cavity, to probe the in-plane field distribution. The homogeneous and circulating nature of the VH mode

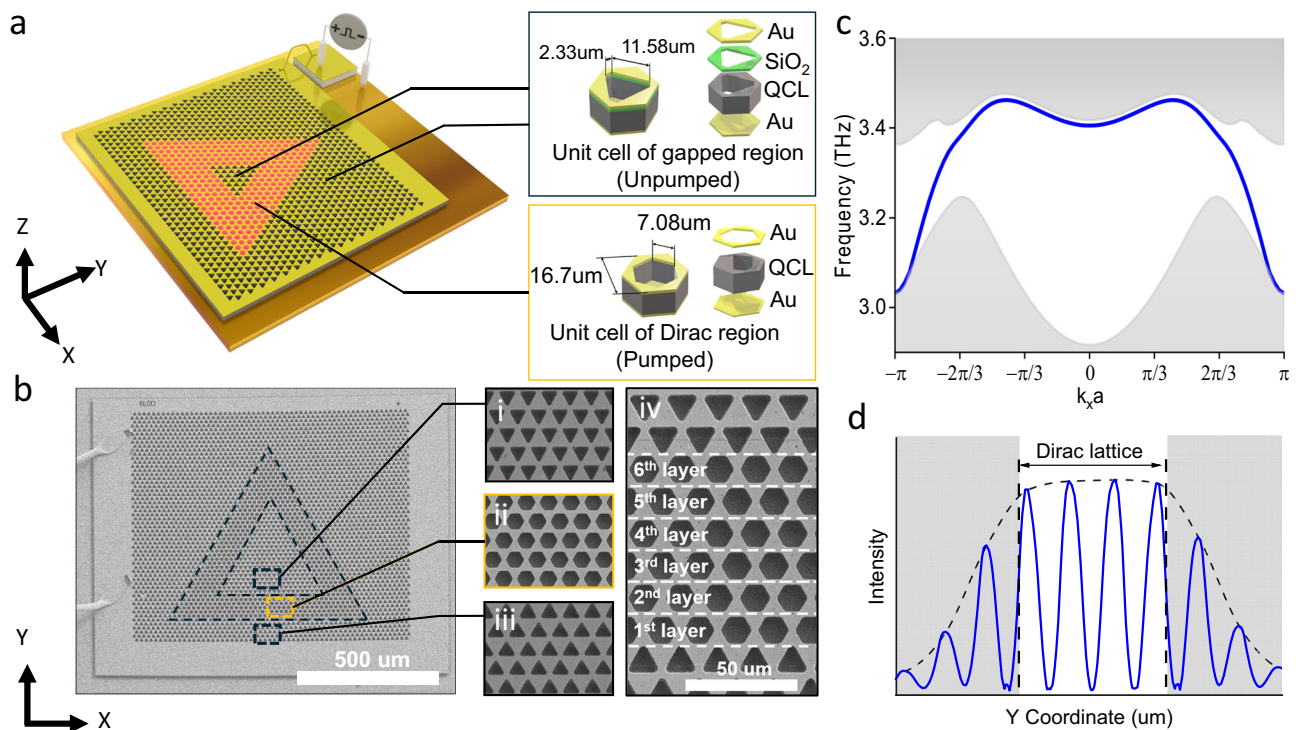


Fig. 1 | Device structure and designs. **a** An illustration of electrically pumped VH THz QCL cavity. The zoom-in diagram indicates the dimension and structure of unit lattice used in various regions of the device. The yellow box highlights the Dirac lattices used in scaling the topological interface. **b** FESEM image of the fabricated device of $D_{Dirac} = 6$. The magnified sub-diagrams in i-iii present the lattice pattern in different regions of fabricated devices, while iv labels the convention of device used

in this work. Here, the constructed waveguide is around 6-unit lattices wide, hence $D_{Dirac} = 6$. **c** Simulated dispersion of the Dirac scaled waveguide. The dispersion of the VH mode is colored in blue while the higher order trivial modes are greyed out for clarity. **d** Illustration of VH mode normalized E-field across the Dirac scaled waveguide. Its mode distribution follows a plateau like envelope in Dirac lattice regions and quickly decays into the gapped region.

in the Dirac-scaled cavity ensures that the defects interact uniformly with the in-plane field, scattering a portion of the radiation towards free space with approximately equal intensity and spectral composition, regardless of the defect's position within the cavity.

To experimentally verify the homogeneity of the lasing mode, a scaled VH cavity with $D_{Dirac} = 6$, $N_{Defect} = 3$, as shown in Fig. 2a, b, was designed and fabricated. The defects were patterned into the QCL simultaneously with photonic crystal airholes using lithography and reactive ion etching (RIE) processes. The simulated normalized electric field of the VH cavity mode in this device is shown in Fig. 2c, where, except in the immediate vicinity of the defects, the VH mode remains evenly distributed without any localization in other regions of the cavity. During characterization, metal cover plates were used to block emission from the other two defects in the cavity, enabling isolated measurements from a single defect. Despite the random placement of the defects, the individually measured scattered emission, shown in Fig. 2d, exhibited nearly identical spectra and intensity. This provides direct evidence of spatial homogeneity and circulating characteristics of the lasing modes within the waveguide of the cavity.

Power scaling

A direct consequence of the enlarged lasing mode volume is the improvement of lasing power. To verify this, we fabricated and characterized three different cavity designs with $D_{Dirac} = 0, 3$ and 6. Surface emission was found to be weaker compared to devices with fabricated defects. This is attributed to the out-of-plane confinement provided by the under-light cone positioning of the VH modes. The simulated VH mode and device structure are shown in Fig. 3a-c, while the experimentally measured light-current-voltage (LIV) curves and maximum detected intensity of each device are presented in Fig. 3d, e. These measurements reveal a clear trend of more than a 10-fold increase in

surface emission as the cavity scales from $D_{Dirac} = 0$ to $D_{Dirac} = 6$. This improved performance is directly attributed to the enhanced interaction between the scaled lasing modes and the QCL active region. As the voltage/current densities increase further (near the right edge of Fig. 3d), a decrease in the output power can be found across all the lasing devices. This phenomenon, also known as the roll-over effect, arises due to intersubband band misalignment in QCLs⁵⁴.

Mode robustness in Dirac-scaled cavity

Unlike systems that break time-reversal symmetry, valley photonic crystals are inherently less robust due to the possibility of intervalley scattering caused by defects³⁹⁻⁴¹. While lasing modes may remain intact with a single defect inside the cavity¹⁹, this resilience diminishes when multiple wavelength-scale defects are present. In such cases, intervalley mixing can lead to standing waves or localization within confined regions of the cavity. While the increased mode volume significantly enhances the mode's robustness against defects along the transmission pathway, as observed in our Dirac-scaled cavity presented in Fig. 2. For controlled comparison with the $D_{Dirac} = 6$, $N_{Defect} = 3$ cavity shown in Fig. 2, we design an unscaled cavity with $D_{Dirac} = 0$, $N_{Defect} = 3$, as shown in Fig. 4a, b. The defect positions and dimensions are similar to those in the $D_{Dirac} = 6$, $N_{Defect} = 3$ cavity, except that they are slightly shifted to the middle of the 1D topological waveguide, where the mode's peak intensity is located. Simulated results for the $D_{Dirac} = 0$, $N_{Defect} = 3$ device are presented in Fig. 4c and Supplementary Fig. 4b in Supplementary Materials. In the simulation setup shown in Supplementary Fig. 4b, c in Supplementary Materials, the VH cavity mode is excited using a directional source to observe the Poynting vector flow within the cavity. In the $D_{Dirac} = 6$, $N_{Defect} = 3$ cavity, the Poynting vector circulate around the defects, while in the unscaled $D_{Dirac} = 0$, $N_{Defect} = 3$ cavity, much of the flow is obstructed.

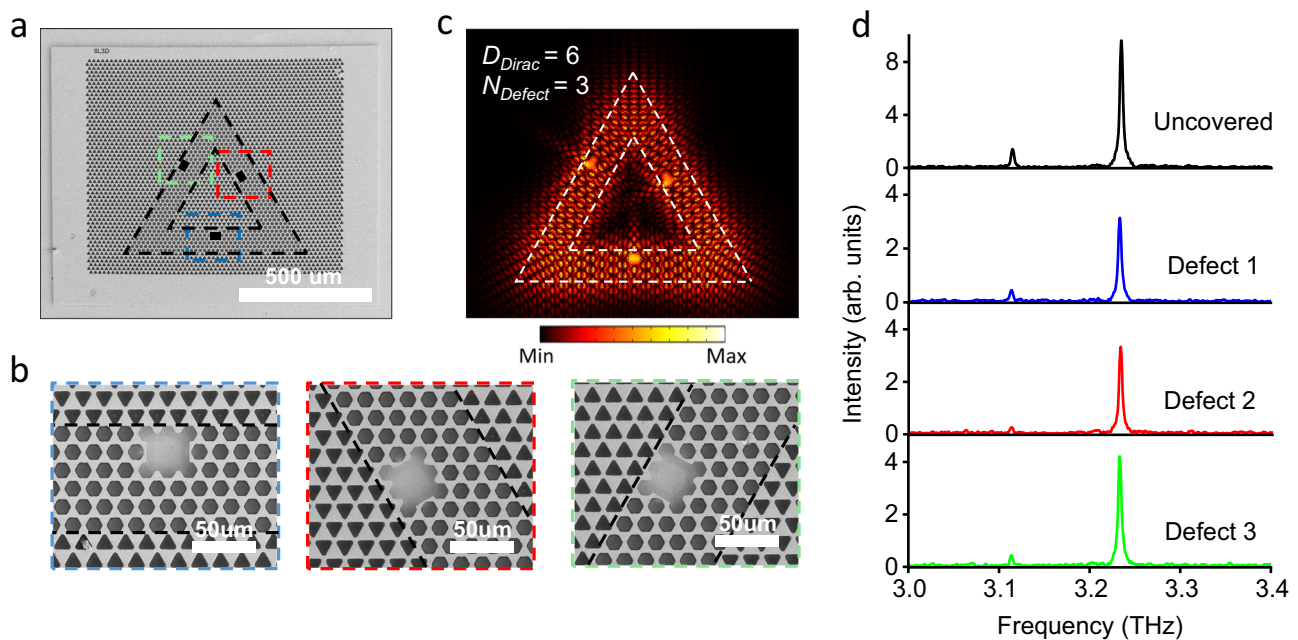


Fig. 2 | Analysis of mode homogeneity in cavity with $D_{Dirac} = 6$, $N_{Defect} = 3$. **a** FEM image with dashed colored boxes highlighting the position of the defect sites within the cavity, while the black triangular dashed lines indicate the boundary of the scaled waveguide. **b** Magnified image for a clearer view of the defect sites within the device. The color of the dashed outline around each picture indicates its respective position in part a of the figure, while the black dashed lines indicate the

boundary of the scaled waveguide. **c** Simulated result of normalized E-Field within the cavity. The boundary of the waveguide is highlighted by white dashed lines. **d** Experimentally measured spectral emissions of the device operating at 0.43 kA/cm². Measurements made without any cover plate is plotted in black, while emissions from individual defect are plotted in their respective color highlighted in part a of the figure.

Examples of the in-gap cavity modes for the $D_{Dirac} = 0$, $N_{Defect} = 3$ configuration are presented in Fig. 4c. The results reveal that the normalized electric field is no longer uniformly distributed and can vary in intensity across different sections of the cavity. This suggests that the defects have induced sufficient perturbation to alter the optical path of the mode. Consequently, scattered emissions from individual defects should exhibit significant variations in both spectral composition and intensity. Using the same defect emission measurement method for the $D_{Dirac} = 6$, $N_{Defect} = 3$ cavity, the experimental results for the $D_{Dirac} = 0$, $N_{Defect} = 3$ cavity reveal inconsistencies in both spectral characteristics and emission intensity, as shown in Fig. 4d.

In addition to comparing with previous VH topological laser designs, we further test our devices against homogeneous Dirac photonic crystals^{45–47}. To this end, we fabricated a control set of THz QCLs with the same sandwiched structure design but with the inner triangular cavity replaced by different photonic crystals (Supplementary Fig. 6). When the Dirac material is not sandwiched between regions of opposite valley Chern number (Supplementary Fig. 6a, b), VH physics is completely removed and the dominant lasing states become localized defect modes. In this case, a similar inconsistent pattern in both spectral characteristics and emission intensity is found for the cover-plate measurements on these Dirac-bulk devices (Supplementary Fig. 6b), indicating that the lasing modes are confined between defects. This set of control experiments emphasizes that topological protection plays an essential role to the robust and extended lasing observed in our design, whereas the Dirac bulk alone does not yield comparable performance.

Discussion

In summary, we have fabricated and systematically characterized a series of VH laser cavity with various degrees of waveguide scaling and defect inclusion. By strategically incorporating in-plane scatters or defects and analyzing their impact through measurement, we verified

that the lasing modes in the scaled cavities are uniformly distributed along and across the waveguide regions formed by Dirac lattices. This spatial uniformity strongly indicates the presence of Dirac-scaled VH mode. Moreover, the measured power output from the devices demonstrated a significant increase with the scaling of the cavity area. Compared to their unscaled counterparts and Dirac-bulk cavity designs, the scaled cavities not only achieved higher emitted power but also enhanced performance in sustaining the lasing mode under varying conditions.

These findings underscore the potential of Dirac-scaled VH cavities to drive advancements across diverse application domains, including photonic integrated circuits, telecommunications, sensing, precision metrology, biomedical and healthcare technologies^{55–57}. The enhanced power output and robustness of these cavities are expected to deliver transformative advancements across these fields, effectively addressing challenges related to power scaling and fabrication imperfections⁵⁸.

Methods

Device fabrication

The 12.8 μm thick QCL active region is processed into a double metal Fabry-Pérot (FP) ridge laser to evaluate its dynamic range, gain profile, and effective index of the waveguide. The growth sheet of the QCL active region could be found in Supplementary Fig. 9 in Supplementary Materials. From the fabricated ridge laser, the active region is estimated to provide sufficient gain for lasing in the range of 3–3.3 THz as shown in Supplementary Fig. 10 in Supplementary Materials, with an effective index of 4.08.

To process the QCL into double metal photonic crystal devices, a bottom electrode consisting of Ti/Au with a thickness of 20 nm/700 nm was deposited on to the QCL and N⁺ GaAs receiving substrate. The gold layers were then bonded together through a thermal compression process at 300 °C for 1 h. The growth substrate was

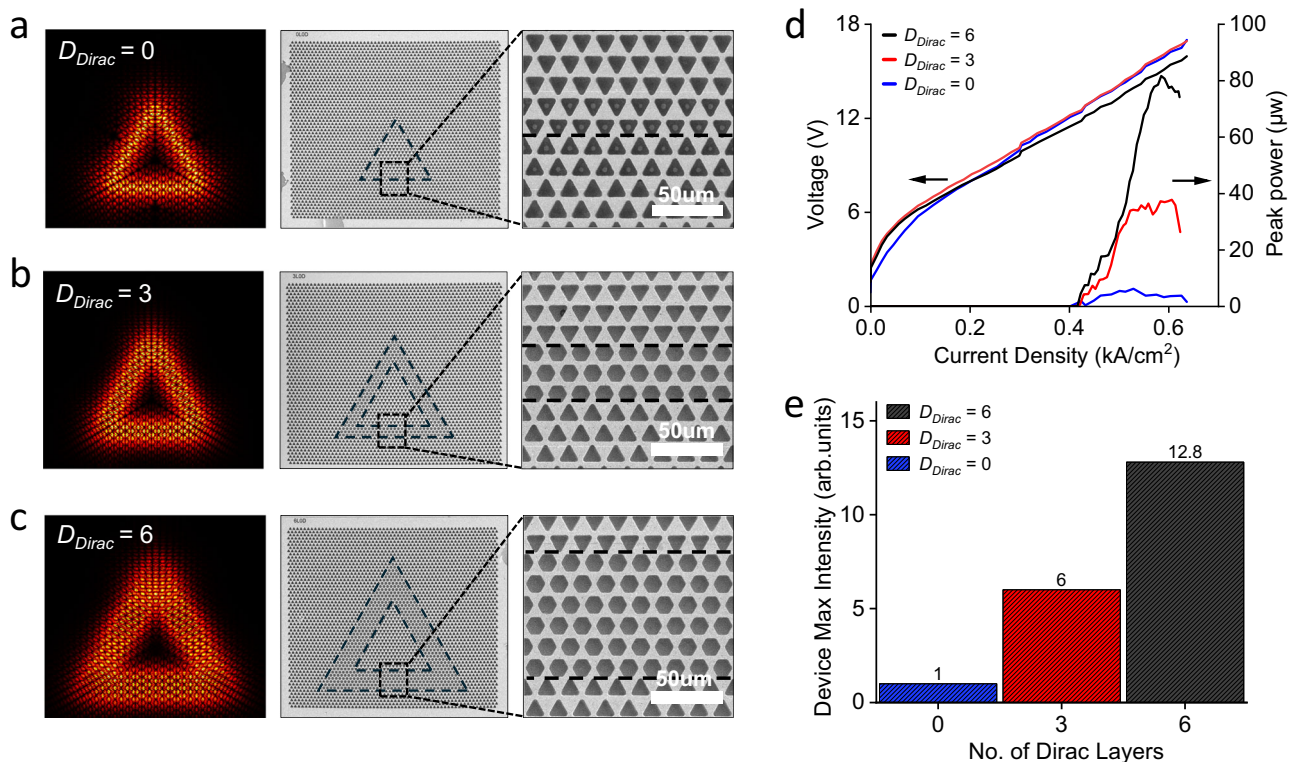


Fig. 3 | Mode scaling and detected power. **a–c** Simulated normalized E-field of VH mode in devices with $D_{Dirac} = 0, 3$ and 6 . The fabricated device of the respective simulation is positioned on the right with a zoom-in diagrams showing details of a section of its waveguide. **d** Experimentally measured LIV of the respective device. The peak output power is not high because our THz QCL wafer is not of high

performance (see Supplementary Fig. 10 in Supplementary Materials). Here, devices with different D_{Dirac} are plotted in their respective color, as denoted by the inset. **e** Comparison of peak power detected from the respective devices in part d of the figure with the power detected from $D_{Dirac} = 0$ normalized as 1.

subsequently lapped down to a thickness of 50 μm , with the remaining substrate removed via selective wet etching. The etch mixture consisted of deionized (DI) water and anhydrous citric acid in a mass ratio of 1:1, respectively. H_2O_2 was then added to the citric acid mixture at a volume ratio of 1:4, respectively. Following the removal of GaAs substrate, a 300 nm etch-stop layer composed of $\text{Al}_{50}\text{Ga}_{50}\text{As}$ was removed using 49% HF acid.

The pump region was defined using 200 nm SiO_2 lithography followed by fluorine-base RIE. This insulating layer reduces the device's current requirements, helping to minimize thermal issues and prevent potential damage to the cavity. Afterwards, the top electrode and hardmask were defined through lift-off lithography, consisting of Ti/Au/Ti/ SiO_2 with thicknesses of 20 nm/400 nm/20 nm /900 nm, respectively. After lift-off, the electrode and hard mask layer adopted the pattern of the photonic crystal design.

The photonic crystal air hole patterns were leveled by RIE, removing 200 nm of exposed SiO_2 insulation above the QCL to ensure proper leveling of the air hole patterns before transferring the photonic crystal design into the QCL using fluorine-base RIE. The process gas used for etching the QCL consists of $\text{Cl}_2/\text{BCl}_3/\text{CH}_4$ at a ratio of 5:100:20 in SCCM. The etch process was terminated once the bottom electrode in the etched region was exposed. The remaining hard mask was removed using RIE. Finally, before gold wire bonding, the chip was cleaved and mounted onto a copper submount using an indium solder.

Characterization

After attaching the chip to a copper submount, the device under test is electrically connected to an electrode using wedge wire bonder. All fabricated devices are characterized within the temperature range of 8.5–9.5 K in a helium-gas-cooled cryostat. Detectable surface emission is measured from the out-of-plane direction of the photonic crystal

device using Bruker Vertex 80 FTIR equipped with deuterated-triglycine sulfate (DTGS) detector. The minimal spectral resolution achievable in the wavelength of interest is 0.08 cm^{-1} .

To power the QCL device, a rectangular pulsed electrical signal at a frequency of 10 kHz with pulse duration of 200 ns is applied. Similar to previous work¹⁹, metal cover plates are used to block unwanted surface emission from the other areas of the device, allowing for the measurement of spectral emission from a particular defect in the waveguide. These plates are positioned and adjusted in close proximity using a 3-axis translator setup mounted onto the cryostat's cold finger where the samples are inserted.

Lasing performance for trivial Dirac-bulk devices

In addition to the Dirac-scaled VH modes, there are several other modes in our cavity which could potentially contribute to lasing. For example, finite-sized Dirac-point bulk hosts band edge mode of high Q-factor, which could lase favorably. To rule out these possibilities, we perform the following control experiments by considering two topologically trivial cavity designs which are:

1. The inner triangle cavity material is replaced with the same material as that of the outer gapped material. Valley Hall physics is completely removed as materials across the interface have the same Valley Chern number.
2. The inner triangle cavity material is replaced with the same Dirac material as that of the interface. Valley Hall physics is also completely removed as now the lasing is dominated by bulk modes closer to the Dirac point of the Dirac material.

In both cases, the dominant lasing modes are now localized modes instead of the running-wave modes for Dirac-scaled VH modes, which result in distinctive lasing behaviours among them. The detailed

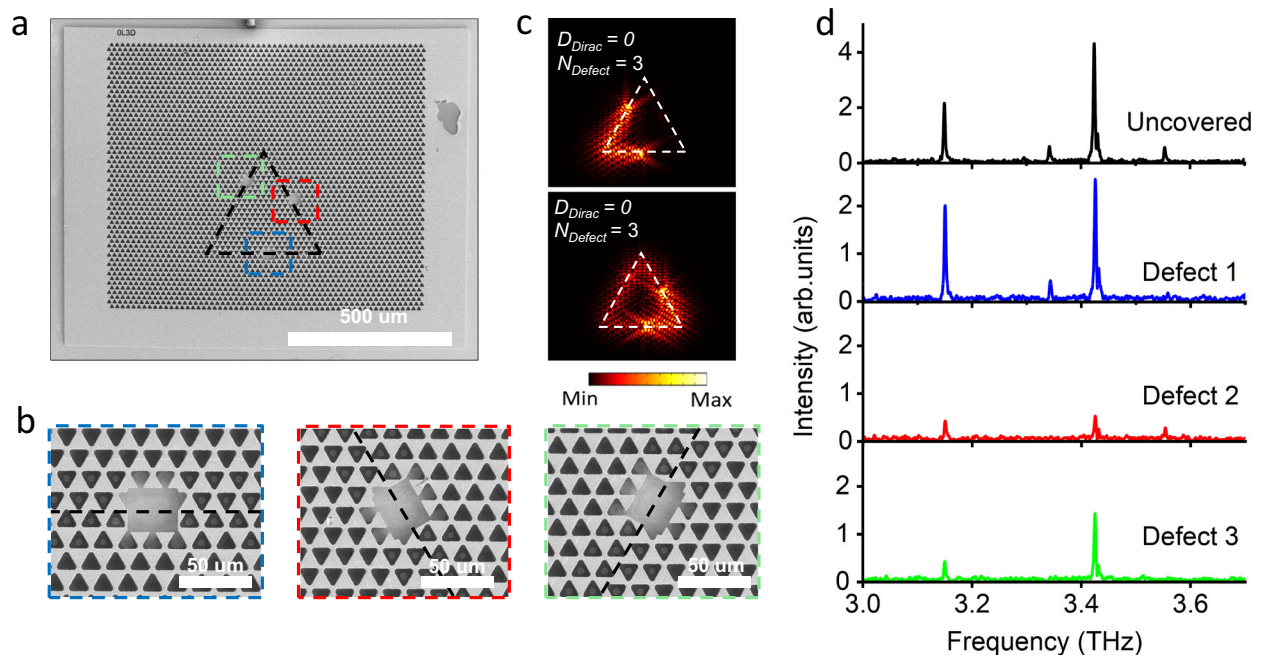


Fig. 4 | Effects of defects in an unscaled cavity $D_{Dirac} = 0$, $N_{Defect} = 3$. **a** FESEM image with dashed colored boxes highlighting the position of the defect sites within the cavity, while the black triangular dashed lines indicate the topological interface of the unscaled waveguide. **b** Magnified image for a clearer view of the defect sites within the device. The color of the dashed outline around the picture indicates its respective position in part a of the figure, while the black dashed line

indicates the topological boundary. **c** Simulated normalized E-field shows that defect is able to significantly disrupt the circulating in-plane mode within narrower waveguide causing localization within the cavity. **d** Experimental measurements of the device operating at 0.53 kA/cm^2 . Measurements made without any cover plate are plotted in black, while measured emissions from individual defect are plotted in their respective color highlighted in part a of the figure.

simulation results can be found in Supplementary Materials. Here, we summarize the experiment results and their comparison with the Dirac-scaled topological design in Supplementary Fig. 6 in the Supplementary Materials.

First, we measure the emission spectrum for these three types of cavities, as shown in the second column of Supplementary Fig. 6. Three distinctive lasing behaviors are observed: the trivial sample exhibits multimode lasing with random mode spacings, as the sandwiched cavity consists of mostly standing-wave modes now. Lasing in the Dirac-bulk sample is dominated by the band-edge mode near the Dirac point, which exhibits nearly single-mode lasing. Lastly, the Dirac-scaled cavity shows regularly spaced lasing peaks, like that being found in the main text.

Second, we consider robustness against defects for the Dirac-bulk and Dirac-scaled cavities in Supplementary Fig. 6b, c. As shown by the cover-plate measurements for the Dirac-bulk sample, most intensity is concentrated close to defect 1 and 3 and the new lasing peaks emerge in addition to the defect-free sample. In contrast, lasing from the Dirac-scaled device shows minimal change, both for the dominant lasing frequency and intensity distribution. This is direct evidence differentiating Dirac-scaled VH modes from the Dirac bulk modes, as the running-mode nature of the former modes prevents it from disorder-induced scatterings.

Last, we compare the emission power from these three designs in Supplementary Fig. 6d. Consistent with the above observations, the Dirac-scaled cavity design provides the largest output power while lasing from the other two control groups delivers far less emission power.

Reporting summary

Further information on research design is available in the Nature Portfolio Reporting Summary linked to this article.

Data availability

The main data supporting the findings of this study are available within the article and its Supplementary Information. Source Data are provided with this paper. All data generated in this study are provided in the Source Data file. Source data are provided with this paper.

References

- Smirnova D., Leykam D., Chong Y., Kivshar Y. Nonlinear topological photonics. *Appl. Phys. Rev.* **7**, 021306 (2020).
- Yan, Q. et al. Advances and applications on non-Hermitian topological photonics. *Nanophotonics* **12**, 2247–2271 (2023).
- Wang, C. et al. Non-Hermitian optics and photonics: from classical to quantum. *Adv. Opt. Photonics* **15**, 442 (2023).
- Li, A. et al. Exceptional points and non-Hermitian photonics at the nanoscale. *Nat. Nanotechnol.* **18**, 706–720 (2023).
- Ozawa, T. et al. Topological photonics. *Rev. Mod. Phys.* **91**, 015006 (2019).
- Kane, C. L. & Mele, E. J. Quantum spin Hall effect in graphene. *Phys. Rev. Lett.* **95**, 226801 (2005).
- Bernevig, B. A., Hughes, T. L. & Zhang, S.-C. Quantum spin Hall effect and topological phase transition in HgTe quantum wells. *Science* **314**, 1757–1761 (2006).
- Thouless, D. J., Kohmoto, M., Nightingale, M. P. & den Nijs, M. Quantized Hall conductance in a two-dimensional periodic potential. *Phys. Rev. Lett.* **49**, 405–408 (1982).
- Raghu, S. & Haldane, F. D. M. Analogs of quantum-Hall-effect edge states in photonic crystals. *Phys. Rev. A* **78**, 033834 (2008).
- Witteck S. et al. Towards the experimental realization of the topological insulator laser. In: *Conference on Lasers and Electro-Optics*. (OSA, 2017).
- Bahari, B. et al. Nonreciprocal lasing in topological cavities of arbitrary geometries. *Science* **358**, 636–640 (2017).

12. Bandres M. A. et al. Topological insulator laser: experiments. *Science* **359**, (2018).
13. Harari G. et al. Topological insulator laser: theory. *Science* **359**, (2018).
14. Klembt, S. et al. Exciton-polariton topological insulator. *Nature* **562**, 552–556 (2018).
15. Smirnova D. et al. Room-temperature lasing from nanophotonic topological cavities. *Light Sci. Appl.* **9**, 127 (2020).
16. Sala, V. G. et al. Spin-orbit coupling for photons and polaritons in microstructures. *Phys. Rev. X* **5**, 011034 (2015).
17. St-Jean, P. et al. Lasing in topological edge states of a one-dimensional lattice. *Nat. Photonics* **11**, 651–656 (2017).
18. Zhao H. et al. Topological hybrid silicon microlasers. *Nat. Commun.* **9**, 981 (2018).
19. Zeng, Y. et al. Electrically pumped topological laser with valley edge modes. *Nature* **578**, 246–250 (2020).
20. Ota Y., Katsumi R., Watanabe K., Iwamoto S., Arakawa Y. Topological photonic crystal nanocavity laser. *Commun. Phys.* **1**, 86 (2018).
21. Hasan, M. Z. & Kane, C. L. Colloquium: topological insulators. *Rev. Mod. Phys.* **82**, 3045–3067 (2010).
22. Faist, J. et al. Quantum cascade laser. *Science* **264**, 553–556 (1994).
23. Köhler, R. et al. Terahertz semiconductor-heterostructure laser. *Nature* **417**, 156–159 (2002).
24. Kumar, S. Recent progress in terahertz quantum cascade lasers. *IEEE J. Sel. Top. Quantum Electron.* **17**, 38–47 (2011).
25. Tonouchi, M. Cutting-edge terahertz technology. *Nat. Photonics* **1**, 97–105 (2007).
26. Zeng Y., Qiang B., Wang Q. J. Photonic engineering technology for the development of terahertz quantum cascade lasers. *Adv. Opt. Mater.* **8**, 1900573 (2019).
27. Han, S. et al. Electrically-pumped compact topological bulk lasers driven by band-inverted bound states in the continuum. *Light Sci. Appl.* **12**, 145 (2023).
28. Han, S. et al. Photonic Majorana quantum cascade laser with polarization-winding emission. *Nat. Commun.* **14**, 707 (2023).
29. Liu, J. et al. High-power electrically pumped terahertz topological laser based on a surface metallic Dirac-vortex cavity. *Nat. Commun.* **15**, 4431 (2024).
30. Xue, H., Yang, Y. & Zhang, B. Topological valley photonics: physics and device applications. *Adv. Photonics Res.* **2**, 2100013 (2021).
31. Schaibley, J. ohnR. et al. Valleytronics in 2D materials. *Nat. Rev. Mater.* **1**, 1–15 (2016).
32. Yang, Y. et al. Terahertz topological photonics for on-chip communication. *Nat. Photonics* **14**, 446–451 (2020).
33. Ma, T. & Shvets, G. All-Si valley-Hall photonic topological insulator. *N. J. Phys.* **18**, 025012 (2016).
34. Gao, Z. et al. Valley surface-wave photonic crystal and its bulk/edge transport. *Phys. Rev. B* **96**, 201402 (2017).
35. Gao, F. et al. Topologically protected refraction of robust kink states in valley photonic crystals. *Nat. Phys.* **14**, 140 (2018).
36. Wang, W. et al. On-chip topological beamformer for multi-link terahertz 6G to XG wireless. *Nature* **632**, 522–527 (2024).
37. Peng, K. et al. Topological valley Hall polariton condensation. *Nat. Nanotech* **19**, 1283–1289 (2024).
38. Jin, F. et al. Room-temperature valley exciton polaritons. *Nat. Comm.* **15**, 10563 (2024).
39. Rosiek, C. A. et al. Observation of strong backscattering in valley-Hall photonic topological interface modes. *Nat. Photonics* **17**, 386–392 (2023).
40. Yu, D., Arora, S. & Kuipers, L. Impact of transforming interface geometry on edge states in valley photonic crystals. *Phys. Rev. Lett.* **132**, 116901 (2024).
41. Kumar, A. et al. Slow light topological photonics with counter-propagating waves and its active control on a chip. *Nat. Commun.* **15**, 926 (2024).
42. Dong, J.-W., Chen, X.-D., Zhu, H., Wang, Y. & Zhang, X. Valley photonic crystals for control of spin and topology. *Nat. Mater.* **16**, 298–302 (2016).
43. Kang Y., Ni X., Cheng X., Khanikaev A. B., Genack A. Z. Pseudo-spin–valley coupled edge states in a photonic topological insulator. *Nat. Commun.* **9**, 3029 (2018).
44. Shalaev, M. I., Walasik, W., Tsukernik, A., Xu, Y. & Litchinitser, N. M. Robust topologically protected transport in photonic crystals at telecommunication wavelengths. *Nat. Nanotechnol.* **14**, 31–34 (2018).
45. Bravo-Abad, J., Joannopoulos, J. D. & Soljačić, M. Enabling single-mode behavior over large areas with photonic Dirac cones. *Proc. Natl Acad. Sci. USA* **109**, 9761–9765 (2012).
46. Chua, S.-L., Lu, L., Bravo-Abad, J., Joannopoulos, J. D. & Soljačić, M. Larger-area single-mode photonic crystal surface-emitting lasers enabled by an accidental Dirac point. *Opt. Lett.* **39**, 2072 (2014).
47. Contractor, R. et al. Scalable single-mode surface-emitting laser via open-Dirac singularities. *Nature* **608**, 692–698 (2022).
48. Li W. et al. Topologically enabled on-chip THz taper-free waveguides. *Adv. Opt. Mater.* **11**, 2300764 (2023).
49. Wang J.-Q. et al. Extended topological valley-locked surface acoustic waves. *Nat. Commun.* **13**, 1324 (2022).
50. Wang, M. et al. Topological one-way large-area waveguide states in magnetic photonic crystals. *Phys. Rev. Lett.* **126**, 067401 (2021).
51. Wang M. et al. Valley-locked waveguide transport in acoustic heterostructures. *Nat. Commun.* **11**, 3000 (2020).
52. Gong, Y., Wong, S., Bennett, A. J., Huffaker, D. L. & Oh, S. S. Topological insulator laser using valley-Hall photonic crystals. *ACS Photonics* **7**, 2089–2097 (2020).
53. Kumar A. et al. Active Ultrahigh-Q (0.2 × 10⁶) THz topological cavities on a chip. *Adv. Mater.* **34**, (2022).
54. Howard, S. S., Liu, Z. & Gmachl, C. F. Thermal and Stark-effect roll-over of quantum-cascade lasers. *IEEE J. Quantum Electron.* **44**, 319–323 (2008).
55. Gupta M., Kumar A., Singh R. Electrically tunable topological notch filter for THz integrated photonics. *Adv. Opt. Mater.* **11**, 2301051 (2023).
56. Wang H. et al. Ultracompact topological photonic switch based on valley-vortex-enhanced high-efficiency phase shift. *Light Sci. Appl.* **11**, 292 (2022).
57. Gu, L. et al. A topological photonic ring-resonator for on-chip channel filters. *J. Lightwave Technol.* **39**, 5069–5073 (2021).
58. Chen, Z. & Segev, M. Highlighting photonics: looking into the next decade. *eLight* **1**, 2 (2021).

Acknowledgements

This work is supported by funding from A*STAR Programmatic Funds (R23IOIRO41, M22K2c0080 (Q.J.W)), the National Research Foundation Competitive Research Program (NRF-CRP23-2019-0007, NRF-CRP29-2022-0003, and the mid-size centre grant NRF-MSG-2023-0002 for National Centre for Advanced Integrated Photonics (Q.J.W)). L.L., A.G.D. and E.H.L. acknowledge the support of the EPSRC (UK) TeraCom programme (EP/w028921/1). At the time this manuscript was under review, we became aware of an independent work (IEEE Journal of Lightwave Technology, 43, 17, 8332–8337, 2025) demonstrating a three-layer Dirac photonic crystal in a valley-Hall topological waveguide. However, that study did not report power scaling or topological protection against defects.

Author contributions

Q.J.W. supervised the work. Y.C., L.Y. and J.C. contributed equally to this work. L.Y. conceived the idea. Y.C. and L.Y. conducted numerical simulation. B.Z. (Bofeng Zhu) provided aid in knowledge application and analysis of the results. Y.C., J.C. and H.L. conducted the fabrication, characterization. The manuscript is drafted and discussed between

Q.J.W., Y.C., L.Y., J.C., B.Z. (Bofeng Zhu) and B.Z. (Baile Zhang). L.L., A.G.D., and E.H.L. performed QCL wafer growth. Q.W. and Z.L. provided assistance with wafer bonding and metrology during fabrication.

Competing interests

The authors declare no competing interests.

Additional information

Supplementary information The online version contains supplementary material available at

<https://doi.org/10.1038/s41467-025-66525-x>.

Correspondence and requests for materials should be addressed to Baile Zhang or Qi Jie Wang.

Peer review information *Nature Communications* thanks the anonymous reviewers for their contribution to the peer review of this work. A peer review file is available.

Reprints and permissions information is available at <http://www.nature.com/reprints>

Publisher's note Springer Nature remains neutral with regard to jurisdictional claims in published maps and institutional affiliations.

Open Access This article is licensed under a Creative Commons Attribution-NonCommercial-NoDerivatives 4.0 International License, which permits any non-commercial use, sharing, distribution and reproduction in any medium or format, as long as you give appropriate credit to the original author(s) and the source, provide a link to the Creative Commons licence, and indicate if you modified the licensed material. You do not have permission under this licence to share adapted material derived from this article or parts of it. The images or other third party material in this article are included in the article's Creative Commons licence, unless indicated otherwise in a credit line to the material. If material is not included in the article's Creative Commons licence and your intended use is not permitted by statutory regulation or exceeds the permitted use, you will need to obtain permission directly from the copyright holder. To view a copy of this licence, visit <http://creativecommons.org/licenses/by-nc-nd/4.0/>.

© The Author(s) 2025